



Full Text View

[Volume 28, Issue 9 \(September 1998\)](#)

Journal of Physical Oceanography

 Article: pp. 1661–1682 | [Abstract](#) | [PDF \(333K\)](#)

Radiation of Energy from Nonzonal Ocean Currents, Nonlinear Regime. Part I: Single Wave Development*

Igor V. Kamenkovich⁺
MIT/WHOI Joint Program, Woods Hole Oceanographic Institution, Woods Hole, Massachusetts
Joseph Pedlosky
Department of Physical Oceanography, Woods Hole Oceanographic Institution, Woods Hole, Massachusetts

(Manuscript received April 21, 1997, in final form October 31, 1997)

DOI: 10.1175/1520-0485(1998)028<1661:ROEFNO>2.0.CO;2

ABSTRACT

The energy radiation from oceanic boundary currents is assumed to be one of the main mechanisms responsible for the production of the highly energetic eddy field in the interior of the ocean. The efficiency of the process is demonstrated in an example of a simple model of a nonzonal flow. The nonzonal orientation of the current proves to be a key dynamical factor setting the radiation in the model.

The effects of the nonlinear interactions on the radiating properties of the solution are studied in detail numerically. The efficient numerical algorithm with open boundary conditions is used. The solutions of the linear problem reported previously by Kamenkovich and Pedlosky are used as initial conditions.

The results show that even rapidly growing linear solutions, which are trapped during the initial stage of development, can radiate energy in the nonlinear regime if the basic current is nonzonal. The radiation starts as soon as the initially fast exponential growth significantly slows. The initial apparent trapping of those solutions is caused by their fast temporal growth. The new mechanism for radiation is related to the nonzonality of a current.

1. Introduction

It is well known that the eddy kinetic energy in the oceanic interior significantly exceeds the energy of the weak background flow in the region of the North Atlantic ([Wyrki et al. 1976](#)). The explanation of the origin of such intensive eddy variability remains an unsolved problem.

One of the possible mechanisms for the eddy generation could be the instability of the background flow itself, which

Table of Contents:

- [Introduction](#)
- [Method of solution and](#)
- [Summary of linear results](#)
- [Mode 1: Zonal jet](#)
- [Slightly nonzonal jet:](#)
- [α = 30°](#)
- [Mode 2](#)
- [Summary](#)
- [REFERENCES](#)
- [APPENDIX](#)
- [FIGURES](#)

Options:

- [Create Reference](#)
- [Email this Article](#)
- [Add to MyArchive](#)
- [Search AMS Glossary](#)

Search CrossRef for:

- [Articles Citing This Article](#)

Search Google Scholar for:

- [Igor V. Kamenkovich](#)
- [Joseph Pedlosky](#)

possesses enough available energy to support the intensive eddy field (Gill et al. 1974). However, whether or not this energy can be entirely released into the eddy motions is a more complicated question. Some numerical studies of the stability of a horizontally uniform baroclinic flow suggest that the eddy energy corresponding to the scales longer than the Rossby deformation radius can exceed the background energy (Larichev and Held 1995; Held and Larichev 1995). In contrast, existing theoretical evidence suggests (Pedlosky 1975) that the mean ocean velocity is a bound for the eddy velocity produced by the baroclinic instability of the oceanic interior.

Energetic boundary currents, such as the Gulf Stream in the North Atlantic, represent an alternative source of the eddy energy. Since in the vicinity of the Gulf Stream up to two-thirds of the eddy energy can be attributed to the meandering Gulf Stream (Halkin and Rossby 1985; Rossby 1987; Hogg 1994), it suggests an effective mechanism for radiation of energy. A swift boundary current can radiate part of its energy into the interior by supporting wavelike motions. Two different approaches to modeling such a process have been tried in the past.

In the first group of studies, the effects of the meandering Gulf Stream are modeled by a zonal, time-dependent rigid boundary (starting with Flierl and Kamenkovich 1975; and Pedlosky 1977). If the meander activity varies in the x direction and has growth and decay periods in time, the energy is effectively transferred to the interior motions and the induced mean circulation in the far field has realistic meridional distribution of eddy kinetic energy (Hogg 1988; Malanotte-Rizzoli et al. 1995). The reader is also referred to Kamenkovich and Pedlosky (1996) for a complete discussion of the results of these studies.

A different approach is needed if we attempt to understand if the radiation is dynamically consistent with the dynamics of the stream itself. In a second group of studies the unstable modes supported by the time-independent basic current are tested for their ability to carry energy to the regions remote from the current axis. Those radiating modes must be very weakly trapped to the current.

Talley (1983) found that zonal eastward parallel flows have difficulty radiating waves. Only zonal jets with some westward components (purely westward, eastward with westward undercurrent, or westward sidelobes) were found to be capable of radiating energy. Only linear solutions are considered in the study.

The fundamental difference between radiating properties of zonal and meridional currents is reported in Fantinini and Tung (1987). It is shown that a simple meridional current can support unstable modes that are radiating.

The next step toward more a complete understanding of the process is made in Kamenkovich and Pedlosky (1996), where the radiating properties of linear instability modes in an ocean current flowing at an angle to the latitude circles are studied. The radiating properties of nonzonal currents are found to be very different from those of zonal flows. For an eastward zonal flow, all solutions are strongly trapped to the jet region. If the jet axis is then tilted by a small angle with respect to the latitude circles, the long and very slowly growing modes become radiating. The radiating ability is further enhanced if the horizontal tilt of the jet axis is increased.

To determine whether a solution is radiating, we use the physically meaningful criterion called the phase speed condition. It states that the frequency and wavenumber of the solution of the linear problem must match those of the free Rossby wave in the far field (see, e.g., Pedlosky 1977; McIntyre and Wessman 1978).

It is, however, often difficult to classify a mode as either trapped or radiating while it is growing rapidly. As indicated in Talley (1983) and in Kamenkovich and Pedlosky (1996), the fast exponential growth of a solution can cause its spatial trapping, therefore disguising its true radiating nature. In that case, one might anticipate that the radiation should start as soon as the fast growth stops. One way to achieve that in the linear theory is to consider the parametric limit of vanishing growth rate along a dispersion curve. If the spatial trapping disappears, we claim that the solutions adjacent to this limit in the parameter space are of a radiating nature.

The linear theory, therefore, gives us very little information about the radiating properties of the solutions that are away from the described limit and grow rapidly, eventually dominating the dynamics in the model. Another way to limit the growth in the model is to consider the nonlinear equilibration during which the fast exponential growth substantially slows. How do the radiating properties in the model change then? To answer this question we formulate here the fully nonlinear problem with the initial state identical to the results from the linear problem in Kamenkovich and Pedlosky (1996). The linear solutions are given very small initial amplitude to ensure their validity during the initial stage of development.

The numerical method used is described in section 2. We also present the method of the analysis of the results in this section. The nonlinear evolution of two linear modes, mode 1 and mode 2, is studied. The reader is referred to section 3 and Fig. 1 for the definition of mode numbers. Mode 1 from the linear barotropic problem is considered in sections 4–6. We first analyze its nonlinear evolution in the model with a zonal current, section 4, and then increase the value of the tilt and concentrate on the effects of the changed orientation. The case of a large tilt ($\alpha = 30^\circ$) is studied in detail in section 6. The dependence of the results on the value of the planetary vorticity gradient is analyzed in section 6c. The nonlinear development of mode 2 is studied in section 7.

2. Method of solution and analysis

The model remains the same as in [Kamenkovich and Pedlosky \(1996\)](#), except that now the nonlinear terms are included into consideration. We assume that the motions are barotropic and quasigeostrophic, and therefore are fully described by the streamfunction ψ , and neglect friction and bottom topography. We study the evolution of the solution that is initially a sum of the basic state $\Psi(y)$ in the form of a nonzonal jet and the linear solutions $\psi(x, y, t)$ with very small amplitudes. The jet is assumed to be uniform in the along-jet direction, and the jet velocity u is zero outside the jet region of finite width $2L_{\text{jet}}$. The model is studied in the rotated coordinate frame. That is, we orient the x axis of our coordinate frame along the jet axis and y axis perpendicular to the jet axis. The equation is then nondimensionalized using the jet half-width L_{jet} and an advective timescale $L_{\text{jet}}/\max(\bar{u})$:

$$\frac{\partial}{\partial t} \nabla^2 \psi + J(\psi + \bar{\Psi}(y), \nabla^2 \psi + \bar{Q}) = \mathcal{F}, \quad (1)$$

where the basic state is given by

$$\bar{Q} = \beta_1 x + \beta_2 y - \bar{u}_y; \quad \bar{\Psi} = - \int \bar{u}(y) dy, \quad (2)$$

with $\beta_2 = \beta \cos \alpha$, $\beta_1 = \beta \sin \alpha$ with α being the angle between our rotated x axis and a latitude circle and β the planetary vorticity gradient.

To balance such a basic state we introduce the potential vorticity source in the equation:

$$\mathcal{F} = -\beta_1 \Psi_y. \quad (3)$$

It is difficult to speculate about the effects that the introduced forcing has on the dynamical properties a priori. However, the results of the particular numerical experiment reported in [section 6c](#) demonstrate that the magnitude of forcing does not control the strength of the energy radiation. The direct effects of the introduced forcing are limited to supporting the basic state.

The nonlinear equation for the time-dependent perturbation streamfunction $\psi(x, y, t)$ is

$$\left(\frac{\partial}{\partial t} + \bar{u}(y) \frac{\partial}{\partial x} \right) \nabla^2 \psi + (\beta_2 - \bar{u}_{yy}) \psi_x - \beta_1 \psi_y + J(\psi, \nabla^2 \psi) = 0. \quad (4)$$

We now need to discuss the form of the initial and boundary conditions. Together they are the decisive factors in choosing the appropriate numerical method of solving (4). For the representation of arbitrary initial conditions, the continuous spectrum of linear Fourier modes is needed and both initial and boundary conditions in x become difficult to formulate. To keep all results simple, we choose to initialize a problem with a single mode with a wavenumber k . The case with a pair of waves will be studied in Part II. Although it is hard to claim that a complete dynamical picture can be obtained by considering either a single wave or a pair of waves, we hope to mimic the important properties of nonlinear interactions and the effects they have on the radiating properties in the problem.

In the course of nonlinear self-interactions, a set of secondary modes that are shorter in x is created in addition to the primary mode: $2k$, $3k$, etc., together with the x -independent component. Because of this special structure of the solution, we can assume periodicity in x with a period equal to the longest period in the set: $2\pi/k$.

The formulation of the boundary conditions in y is more difficult. The conditions need to remain the same as in the linear problem and be equivalent to the analytical condition of boundedness at $\pm\infty$. However, it is not easy to implement such conditions numerically. Ideally, one should require that any disturbance that approaches the numerical boundary in y , which is typically more than seven jet widths away from the jet axis, should be able to leave the domain without even partial reflection.

One way to allow free transmission of a wave through the boundary is to use modified Orlandi boundary conditions ([Orlandi 1976](#)). At the boundary in y , we write

$$\frac{\partial}{\partial t} \psi + c(x, y, t) \frac{\partial}{\partial y} \psi = -\psi \frac{1}{T_f}. \quad (5)$$

The speed c , with which a disturbance propagates, can be calculated numerically and is used to determine ψ at the boundary. We also introduce the numerical damping on the right-hand side of the above equation. The term controls the

numerical instability at the boundaries (Blumberg and Kantha 1985). For all our computations we choose $T_f = 1$, which is sufficient for the above condition to work well in our case. The finite-difference form of the conditions is given in the [appendix](#).

The next important task is to convince ourselves that the conditions actually work. We check that by first changing the size of our numerical domain. If the results do not change, we are convinced that the boundary effects, such as a reflection or the amplification of the boundary-trapped numerical modes, are minimal. Otherwise the solution would depend on the size of the numerical domain. We normally stop the integration at the point when we suspect growing boundary effects.

We then choose the numerical method for the solution that is the most efficient given the boundary conditions just formulated. We use a rectangular basin with N_x points in x and N_y points in y , where N_y is typically larger than N_x . The grid spacings are Δx and Δy correspondently. [Equation \(4\)](#) for the vorticity is time stepped forward using the leapfrog scheme. The resulting ζ is then inverted to obtain streamfunction ψ .

a. Analysis of results: Fourier components

The solution obtained by the method outlined above has a complicated structure. As was noted in the previous section, several Fourier components in x are created in the course of nonlinear development. Because the solution is periodic in x , it is possible to perform the decomposition into Fourier series:

$$\psi(x, y, t) = \text{Re} \sum_{n=0}^{\infty} \Phi_{k_n}(y, t) e^{ik_n x}, \quad (6)$$

where

$$\Phi_{k_n}(y, t) = \frac{1}{L_x} \int_0^{L_x} \psi(x, y, t) e^{ik_n x} dx$$

are the Fourier coefficients and $k_n = 2\pi n/L_x$.

When we use the term, for example, “component ‘0.25,’” it will mean the Fourier component with $k_n = 0.25$ and corresponding coefficient $\Phi_{0.25}$.

At the very beginning of the development, when only a single linear wave of the general form $\Phi(y) e^{ik_n(x-c_n t)}$ is present, we have

$$\Phi_{k_n}(y, t) = \Phi(y) e^{-ik_n c_n t}.$$

Other Fourier coefficients grow in time due to the nonlinear interactions that produce new components, representing the temporal evolution of spatial structure. As we noted in the previous section, only a few of them are significant. Secondary components “0,” “ $2k_n$ ” are created by the self-interactions of the initial wave with $k = k_n$. Components “ $3k_n$,” “ $4k_n$,” etc., emerge later as a result of secondary interactions.

The Fourier representation of solution [\(6\)](#) possesses another convenient property. If we compute the x -averaged kinetic energy using [Eq. \(6\)](#), we find

$$\begin{aligned} K_e &= \sum_{n=0}^{\infty} K_{k_n} \\ &= \int_{-\infty}^{\infty} \frac{1}{2} \Phi_{0y}^2 dy + \sum_{n=0}^{\infty} \frac{1}{4} \int_{-\infty}^{\infty} (\Phi_{k_n y}^2 + k_n^2 \Phi_{k_n}^2) dy. \quad (7) \end{aligned}$$

All terms that are x -dependent disappear because of the x -averaging over the interval $[0, L_x]$. We see that the contributions of each component to the total perturbation kinetic energy are additive. The property is convenient for analyzing the energetics in the problem. By analyzing the values of K_{k_n} , we will be able to see which components contribute the most to the total value of K_e .

In the analysis of the energetics in the problem we will use another quantity that is the kinetic energy of each component

$$\frac{1}{4}(\Phi_{k_n y}^2 + k_n^2 \Phi_{k_n})$$

integrated from $-\infty$ to -2 and from 2 to $+\infty$. We therefore exclude the region that contains the jet itself ($\bar{u} \neq 0$ for $-1 < y < 1$) and thus include only the energy appearing well outside the region of the basic current. We will denote this value by E_{k_n} and will consider its ratio to the total perturbation energy K_e . The ratio serves as the measure of the effectiveness of radiation by each component. It is a more meaningful quantity than the absolute value of E_{k_n} since the latter strongly depends on initial conditions and would be hard to use in the comparison between different cases.

For evaluation of the integral over the infinite interval in y , we will use the integration over the numerical interval.

3. Summary of linear results

Before we proceed with the analysis of the nonlinear evolution of the solutions of the linear problem, we briefly present the linear results themselves. The reader is referred to [Kamenkovich and Pedlosky \(1996\)](#) for the complete discussion.

Two unstable modes (mode 1 and mode 2 hereafter) are found. The dispersion curves showing the phase speeds c_r and the growth rates θ_i as functions of the x -wavenumber k are shown in [Fig. 1](#) for different values of the horizontal tilt α of the jet axis.

In the case of a zonal jet, all solutions are strongly trapped to the jet region. Mode 1 is a varicose mode with the streamfunction antisymmetric in y and mode 2 is a sinuous mode with a symmetric streamfunction. When α is different from zero, the waves with wavenumbers close to the long-wave cutoffs of either of the modes become radiating in the cross-jet direction.

The short waves of each of the modes are trapped due to their fast exponential growth in time. In what follows, we mainly discuss the results for those short and trapped waves, concentrating on the changes in their radiating properties in the course of nonlinear development.

4. Mode 1: Zonal jet

We start the analysis with the study of the nonlinear development of a single mode in the case of a zonal current, $\alpha = 0^\circ$. The linear theory predicts the strong spatial trapping of all solutions for all wavelengths. Does the solution remain trapped during the nonlinear development as well?

We initialize the problem with a linear varicose mode for $k = 1$ and $\beta = 1$. We now proceed with the analysis of the numerical results. We carry out the computations over a time interval of 112 nondimensional units. The nondimensional e-folding timescale is 7.5 according to the linear theory. The equilibration begins at $t > 32$.

The 1D plots of the perturbation streamfunction versus y for a fixed value of x are shown in [Fig. 2](#). The solution is trapped initially in the agreement with the linear theory and is antisymmetric in y since we consider a varicose mode. We now remark that the nonlinear interactions cannot change the antisymmetry of the solution because nonlinear terms in the equation $J(\psi, \nabla^2 \psi)$ are antisymmetric if ψ is antisymmetric itself. In other words, the solution should remain antisymmetric for all times.

Nevertheless, we observe the change in the structure of the solution for $t > 64$. The strong symmetric component of the solution is present, and it amplifies even further for later times. In addition, we observe a wavelike response in the exterior region that reaches far from the jet at $t > 96$. Do we see the influence of an additional strongly unstable symmetric mode?

The analysis of the Fourier components of the streamfunction helps to clarify the picture. Components “0,” “1,” and “2” are shown in [Fig. 3](#). The problem is initialized at $k = 1$; the component “1” is much larger in amplitude than component “2” for $t \leq 48$. The latter is antisymmetric in y and, therefore, remains to be mainly produced by the nonlinear self-interactions of component “1.”

The situation changes at later times. At $t = 64$, the component “2” is practically symmetric and is almost the same amplitude as component “1”; it further amplifies with time. We can conclude that starting from $t = 64$, the sinuous mode with $k = 2$ dominates the development ($t = 80$). The sinuous mode at $k = 2$ is the most unstable wave in the problem; in particular, it has a growth rate twice as big as that of a varicose mode for $k = 1$ (see [Fig. 1](#)). The wave is most likely initialized by the presence of roundoff numerical error in the numerical method during the development of the component “2” created by the self-interactions of mode 1.

In a numerical experiment not presented here, we put the sinuous mode with $k = 2$ in addition to the varicose mode as an initial condition. The sinuous mode initially has much smaller amplitude (by a factor of 350). The nonlinear development is

very similar to that observed in the numerical run with a varicose mode. Thus, the present calculation mimics the production of the sinuous mode in the previous experiment with a single varicose mode. In the present calculation, the sinuous mode shows up earlier as if in a more advanced stage of nonlinear development.

We now come back to the experiment with a single varicose mode. What is also interesting to see is that the primary component “1” starts to decrease in amplitude after $t = 64$. The amplitude of component “1” reduces by a factor of 10 from $t = 64$ to $t = 96$. Simultaneously it radiates away waves from the jet region to which it is initially trapped. The whole process looks as a transition from the development of the single varicose mode “1” to the development of the single sinuous mode “2.” During the transition, the component “1” gives way to the component “2” and radiates away the energy that it previously gained during the initial unstable growth. The radiation is of transient nature and has very small amplitudes.

One should also note the presence of the component “0”; its significance will be discussed in detail in the following sections. The x -independent component remains trapped throughout the whole process of nonlinear development.

The next plot, [Fig. 4](#), shows the energy corresponding to each Fourier component. We see that component “2” starts to dominate the process after $t = 64$; integrated over the whole domain, energy corresponding to this mode K_2 is the largest after that time ([Fig. 4a](#)).

The balance is very different if the energy for each component is integrated everywhere except the region $[-2, 2]$, which contains the jet itself. The component “1” is clearly dominant in the external region defined above; see [Fig. 4b](#). The ratio E_1/K_e further increases after the beginning of the radiation by this component. However, the radiation is not energetic; E_1 is about 1 percent of the total kinetic energy K_e . The contribution of the other components to the external kinetic energy is much smaller.

The transient radiation reported in this case is very closely related to the radiation by pulsating meanders discovered in a series of zonal boundary forced models ([Malanotte-Rizzoli et al. 1987](#); [Hogg 1988](#); [Malanotte-Rizzoli et al. 1995](#)). In these studies, it is demonstrated that the growth and decay periods in the life cycle of meanders are essential for the mechanism discovered. In our case, the radiation in the form of component “1” starts at an advanced stage of nonlinear development, when component “1” starts to decay in amplitude. The decay follows the period during which the component remains trapped to the jet region and has a large amplitude, therefore representing meanders of the jet with nondimensional wavelength 2π . Thus, the slow decay of these meanders can produce radiation in accord with the mechanism described in [Malanotte-Rizzoli et al. \(1987\)](#), [Hogg \(1988\)](#), and [Malanotte-Rizzoli et al. \(1995\)](#). The mechanism, however, is not very effective in our case. The radiation is very weak, in part as a result of the smallness of component “1” in the jet region.

5. Slightly nonzonal jet: $\alpha = 5^\circ$

We now increase the value of the horizontal tilt from zero to the small value of 5° . We recall from [Kamenkovich and Pedlosky \(1996\)](#) that the linear solution changes its radiating properties qualitatively. The slowly growing long waves in the model become radiating, whereas the shorter linear waves remain trapped during the linear stage of development. Do the radiating properties of short waves change in the course of nonlinear development?

To answer this question, we initialize the problem with mode 1, which is the modified varicose mode of the zonal jet for $k = 1, \beta = 1$. According to the linear theory (see [Kamenkovich and Pedlosky 1996](#)), the solution for this choice of k is strongly trapped.

One-dimensional plots of the streamfunction are presented in [Fig. 5](#) for a chosen value of x . The observed dynamical picture is similar to that in the case of $\alpha = 0$. The strong symmetric component is clearly seen in the structure of the solution at $t > 48$, and the radiation starts later. These facts suggest the presence of the dynamical process described in the preceding section in which the interactions between the initially posed varicose mode and the excited, later highly unstable, sinuous mode cause the former to radiate. For the linear problem with the tilt as small as 5° the results are almost the same as for the zonal jet unless a wave is very long in x ; see [Fig. 1](#) and [Kamenkovich and Pedlosky \(1996\)](#). It is not therefore surprising to find the nonlinear behavior in both cases similar as well.

However, some important differences with the case $\alpha = 0$ are obvious. First of all, the radiation starts much earlier, at $t > 40$. The amplitude of the radiating response is larger than that in the case $\alpha = 0^\circ$ and has more complicated structure. Do we now observe the new mechanism for radiation of short waves related to the nonzonality of the current at work here? To give a detailed answer to this question, we now consider the Fourier coefficients Φ_{k_n} in [Fig. 6](#). The comparison of this plot with [Fig. 3](#) reveals a significant difference in the dynamical development.

1) The radiation in the exterior region now starts as early as $t = 40$ and initially is in the form of x -independent component “0” (Φ_0). The component represents the change in the x -averaged momentum. Well-pronounced radiating properties of the component “0” will be observed for all numerical experiments as long as the tilt is nonzero. The reason for the component “0” radiating more easily than other components can be illustrated by a simple example.

Imagine the forced-boundary problem in which the boundary is x independent and oscillates with a given frequency ω . No

linear wavelike solution is possible if the boundary is oriented zonally. However, Rossby waves can exist if the boundary is tilted. The dispersion relation for the response in the rotated coordinate frame is then

$$\omega = \frac{\beta_1}{l}.$$

If the frequency of the boundary oscillations ω is complex (the magnitude of oscillations is growing in time), then l is complex as well and solution decays away from the boundary. As long as ω is purely real, the response is a plane wave *regardless* of the value of the frequency. In other words, the only reason for the spatial trapping of the solution is its exponential growth in time. No additional constraints on the value of the frequency analogous to the phase speed condition (Kamenkovich and Pedlosky 1996; see also next section) exist.

The other property of this simple example is that the group velocity in the y direction is single signed:

$$c_{gy} = -\frac{\beta_1}{l^2}.$$

Since the c_{gy} is always negative, the linear radiation from the boundary can only exist for negative y . One can see that this holds true in our case for $\alpha = 5^\circ$. In Fig. 6 we observe that component “0” initially radiates only to the left from the jet region. The radiation to the right starts later, most likely as a local result of nonlinear interactions in the exterior and is not directly forced by the jet edge.

2) Component “1” (Φ_1) radiates for $t > 64$ and remains at least as large as Φ_2 . Its amplitude does not decrease with time as it happens for $\alpha = 0^\circ$. The radiation therefore does not simply accompany the transition from the mode 1 to mode 2 but rather is a robust feature of the late stage of the development of component “1.”

3) The radiation is also more energetic now, as we can see in Fig. 7. The external part of the energy corresponding to the component “1” is now approximately 2.5% of the total perturbation energy. One percent of the total energy is radiated into the exterior by each of the components “0” and “2.” The sum of these numbers, $(E_0 + E_1 + E_2)/K_e$, is 4.5%, which is much bigger than the same quantity for $\alpha = 0^\circ$ (dotted line in Fig. 7). The more energetic radiation in the case of the slightly nonzonal current is apparent.

The described radiation for $\alpha \neq 0$ is different from the weak transient radiation in the case of the zonal jet. The radiation is more energetic and occurs much earlier in the case of a nonzonal jet. The radiating response has complex structure and does not weaken with time.

6. $\alpha = 30^\circ$

We now turn our attention to the analysis of the development of a short wave, $k = 1$ in the case of a large tilt. The comparison of the following results with the results from the previous sections 4 ($\alpha = 0^\circ$) and 5 ($\alpha = 5^\circ$) for the same k will help us to understand the dynamical effects of the nonzonality.

The logarithm of $K_e(t)/K_e(0)$ is shown in Fig. 8 by the solid curve. One can see that the solution grows in agreement with the linear theory initially since the curve is very close to the dashed line showing the linear growth $2\omega_1 t$. Then the growth begins to slow at $t > 16$, significantly decreases by $t = 40$, and the curve starts to oscillate reaching the period of relatively slow growth. We will call the second phase of development associated with the small growth rate ($t > 40$) the nonlinear equilibration, although the solution does not reach a steady state.


We now analyze the energy budget in the problem. The zonally averaged perturbation energy equation integrated in y from $-y_b$ to y_b takes the form


$$\frac{\partial}{\partial t} K_e(y_b) = \int_{-y_b}^{y_b} \overline{u_y \psi_x \psi_y} dy + \left[\overline{-u \psi_x \psi_y} + \overline{\psi \psi_{yt}} - \frac{1}{2} \beta_1 \overline{\psi^2} - \frac{1}{2} \overline{\psi^2 \nabla^2 \psi_x} \right]_{-y_b}^{y_b}, \quad (8)$$

where a horizontal bar represents averaging in x and

$$K_e(y_b) = \int_{-y_b}^{y_b} \frac{1}{2} \overline{(\psi_x^2 + \psi_y^2)} dy.$$


Flux terms on the right-hand side of the above equation should vanish at infinity ($y_b = \infty$), leaving the above equation in the form of a balance between the energy production term F_{brt} and the rate of change of energy. At the boundaries of our numerical domain, flux terms typically remain negligible until the end of each experiment. Note also the absence of an energy source directly related to the forcing.

We plot all three terms as functions of time for a region twice as wide as the jet itself in [Fig. 9](#) . We observe the almost perfect balance between the term F_{brt} and the rate of change of energy until $t = 40$, after which time the energy flux terms become significant. In fact, at $t = 40$ the flux exactly balances the rate of change of the perturbation energy. The flux is always negative indicating the outflow of energy from the region. Does it indicate the beginning of radiation at this stage?


We observe the evolution of the structure of the solution in the 2D contour plots of the total streamfunction $\Psi(y) + \psi(x, y)$ ([Fig. 10](#) ). The full flow field is noticeably different from the basic state starting at $t = 16$. The initially parallel basic flow is strongly modified by the presence of meanders that are trapped to the jet region. The dominant wavenumber of those meanders is $k = 1$ since the width of the numerical region L_x in the x direction apparently equals two wavelengths and $2 \times 2\pi/L_x = 1$.

The solution remains trapped until $t = 32$. The perturbation field extends in the cross-jet direction for later times: $t > 40$. We remember that time $t = 40$ corresponds to the transition from fast exponential growth to the phase of the very slow rate of increase in the kinetic energy. Therefore, we observe radiation beginning at the moment when fast growth significantly slows.


For negative y , eddies elongated in the x direction are formed in the far field by the end of the numerical experiment ($t = 72$). For positive y , the eddies are elongated in the direction that makes an angle to the jet axis, which, in turn, is tilted itself. The heavy dashed lines in the figure parallel to the latitude circles give us an idea about the orientation of these eddies in the conventional, nonrotated coordinate frame. As we can see from the figure at $t = 72$, the eddies for positive y are oriented nearly east–west, demonstrating the asymmetry of the dynamical field in the cross-jet direction.


We now analyze the 1D plots of the streamfunction in [Fig. 11](#)  , which provide us with additional information about the structure and the amplitudes of perturbation motions. The amplitude of the wavelike radiating response in the exterior grows in time after the start of radiation at $t = 40$. We can see that by $t = 56$ the perturbations with large amplitudes have filled the entire numerical domain, which is 15 times wider than the jet itself. What we observe is the process that effectively transfers energy from the energetic unstable current to the remote exterior regions. The importance of this process requires a detailed study.

At first glance, the structure of the radiating response appears complex. What is the detailed structure of the obtained solution? Is mode 2 excited the way it is in the previous numerical experiments for $\alpha = 0^\circ$ and $\alpha = 5^\circ$ and, if so, what is its role now? We note that even if $\alpha = 30^\circ$, short linear waves in the problem are still easy to identify as modified symmetric (mode 2) and antisymmetric (mode 1) modes of a zonal jet, which simplifies the answer to the last question.

We present the Fourier coefficients as functions of y in [Fig. 12](#)  for certain chosen times. The overall dynamical picture is similar to that for the case with $\alpha = 5^\circ$. The radiation starts in the form of an x -independent component Φ_0 after $t = 40$ and takes place mainly in the half-plane where y is negative. The component represents the change in the x -averaged velocity field; it reaches large amplitudes for $y > 0$ at later times.

The component “1” starts to radiate immediately following component “0.” The amplitude of the radiating response in both the exterior regions is almost as large as that inside the jet region $[-1, 1]$. In contrast, component “2” mainly radiates for positive y .

As in previous cases, we also find nearly symmetric $\Phi_2(y)$ at $t = 40$. It is the sum of the very unstable nearly symmetric mode 2 that is generated due to the numerical noise in the problem and the presence of the secondary component produced by self-interactions of component “1,” which is antisymmetric. The symmetric structure in the interior points to the dominance of mode 2 in component “2” in the region. However, despite the large growth rate (see [Fig. 1](#) ) of mode 2 for $k = 2$, component “2” is never larger than the component “1” and does not dominate the development. The amplitude of component “1” remains the largest in the set.

We now consider plots of the kinetic energy calculated for each component ([Fig. 13](#) ). The values of K_n integrated over the whole domain are shown in the upper panel. Component “1” is very important energetically; unlike the case with $\alpha = 0$, component “2” does not dominate the late stage of the development.

In the lower panel, the external kinetic energy E_n is divided by K_e to give the portion of total energy that is contained in both the regions $[-\infty, -2]$ and $[2, \infty]$. The picture further emphasizes the efficiency of the radiation from a nonzonal current now enhanced by the large tilt. The plotted values are very small before the beginning of the radiation, approximately at $t = 40$. After this time, we observe the increase in the radiated energy associated mainly with the component “1.” More than

17% of K_e is radiated by this component by the time $t = 72$.

The components “0” and “2” contribute approximately 10% and 6% of K_e to the total value of the external energy. The x -independent component of the solution has large amplitudes; its contribution to the kinetic energy is however smaller, mainly because of the zero \mathbf{U} velocity associated with it.

We can conclude that the mechanism that causes the solution to radiate as soon as its growth becomes very slow is much more effective compared to the relatively weak transient process of radiation found in the case of $\alpha = 0$. More than 30% of K_e is eventually transferred into the external regions at $\alpha = 30^\circ$. The ability of short waves to radiate is related to the change in their dynamical nature related to the nonzonal orientation of the current. The change is the strongest for slowly growing solutions; in the linear problem, it can only be observed for long waves. Nonlinear effects stop the growth and enable short waves to radiate.


a. Component phase speed

One of the most important criteria for radiation that we used in the linear problem was the phase speed condition that requires that the frequency and wavenumber of the linear solution match those of the free Rossby wave in the far field (see, e.g., [Pedlosky 1977](#); [McIntyre and Wessman 1978](#)). The condition, therefore, sets the limits on the phase speeds of a radiating wave ([Kamenkovich and Pedlosky 1996](#)):

$$-\beta \frac{(1 + \cos\alpha)}{2k^2} < c < \beta \frac{(1 + \cos\alpha)}{2k^2}. \quad (9)$$

It is hard to apply the same condition to the finite amplitude solution everywhere in the domain because solution is no longer a wave with well-defined phase speed. However, it may be relevant to the radiating response in the exterior. The motions there have small amplitudes during the beginning phase of radiation and should be nearly in a linear balance locally. As long as the amplitude of a Fourier coefficient is small, we can define the phase speed for each Fourier component through the time derivative of the complex phase:

$$c_{k_n}(y, t) = -\frac{1}{k_n} \frac{\partial}{\partial t} \arctan\left(\frac{\text{Im}\phi_{k_n}(y, t)}{\text{Re}\phi_{k_n}(y, t)}\right). \quad (10)$$

It is easy to check that in the case of a plane wave, the above relation gives the correct constant phase speed. In our nonlinear problem, the phase speed defined by (10) is generally a function of time and y , but should be close to the constant value if Φ_{k_n} is nearly in the linear balance. The values c_1 computed for the component “1” are presented in [Fig. 14](#) .


At $t = 16$ the solution is still practically linear and the phase speed is very close to constant. Its value lies outside the interval set by the phase speed condition (9), which implies spatial trapping according to the linear theory. The propagation of the phase slows at later times; in fact, c_1 at $t = 8$ is already smaller than that for the linear solution. At $t = 40$, which is the beginning of the strong radiation in the model, c_1 satisfies the phase speed condition (9), which is the necessary condition for radiation in the linear problem. The phase speed is mostly negative and small in absolute value.

The solution in the exterior at $t = 40$ is still nearly linear because of its small amplitude. As a result, the phase speed calculated using [Eq. \(10\)](#) is reasonably close to the constant in the region $-3 < y < -1$ and for positive y . Therefore, the beginning of radiation is dynamically consistent with the linear theory. The phase speed c of the initially trapped solution decreases due to the nonlinear effects, and the radiating response starts to develop as soon as c becomes small enough to satisfy the phase speed condition.

The situation changes for later times: c strongly depends on y at $t = 64$, which can be explained by the nonlinear nature of the radiating response. The phase speed still satisfies the phase speed condition; however, the analogy with the linear-boundary-forced problem is difficult to draw in this case.

b. Long wave: $k = 0.25$

As can be seen from [Eq. \(4\)](#), the influence of the x component of the planetary vorticity gradient $\beta_1 = \beta \sin\alpha$ is the strongest for waves long in x . Indeed, in the long-wave limit all x derivatives become smaller and the significance of the term $\beta_1 \Psi_y$ in [Eq. \(4\)](#) increases. The results for a long wave presented below should therefore emphasize the effectiveness of the mechanism for radiation related to nonzonal as it is described in the preceding sections.

We choose our initial conditions in the form of a single linear wave for $k = 0.25$, $\beta = 1$, and $\alpha = 30^\circ$. Despite that its growth rate is almost half that of the wave with $k = 1$, the wave still grows rapidly (see [Fig. 1c](#) ). As a result, the solution initially should be trapped.

The Fourier coefficients are presented in [Fig. 15](#). We observe that $\Phi_{0.25}$ is, indeed, weakly trapped during the very early stage of development. The radiation further develops at later times when nonlinear effects cause other components of the solution to emerge.

Component “0” reaches finite amplitudes at $t = 40$, and the radiation starts quickly after that and occurs initially to the left from the jet region only ($t = 64$). Component “0.5” produces radiation as vigorous as that produced by the component “0.25” ($t = 64$). The radiation is very dramatic at later times; see [Fig. 15](#) for $t = 88$. All three components correspond to the very energetic radiation in the exterior region. The process of the transfer of energy from the jet to the remote in the cross-jet direction regions is very effective.

The effectiveness of the aforementioned transfer of energy is further outlined by the values of the ratio of the external part of energy E_{k_n} to the total perturbation energy K_e (see [Fig. 16](#)). The component “0.25” dominates the radiating response initially since the linear wave used as the initial condition is only weakly trapped. The corresponding energy in the external regions increases in absolute value together with the kinetic energy integrated over the whole domain. As a result, the ratio between two values increases only slightly in the course of nonlinear development.

In contrast, the relative importance of other components rapidly grows in time. As a result, the energetically significant part of the spectrum is broad in the described numerical experiment. By the time $t = 96$, component “0” gives 5% and component “0.5” gives 8%.

Short waves are very energetic in the described experiment. Their wavenumbers correspond to large growth rates in the linear problem (see [Fig. 1](#)). The secondary harmonics created by the nonlinear interactions can in turn cause the growth of unstable linear modes for the same wavenumbers because of the roundoff error in the numerical method. The anticipated process is similar to the excitation of mode 2 in the preceding section and can explain the widening of the spectrum in the described case.

The secondary harmonic “1.25” contributes almost as much as the primary component “0.25” to the value of the external energy. Component “0.75,” which is excited by the secondary interactions between components “0.25” and “0.5,” quickly overcomes the latter in terms of corresponding energy in the external region. Its external portion of energy is almost 14% of the K_e by the end of the numerical experiment.

One should expect the structure of the radiating response to become more complex in the course of further development with a larger number of short waves forming. One fact that will hold true is the remarkably energetic radiation. Indeed, if we add individual contributions of each the component presented in the plot together, we get almost 70% by $t = 96$! (Compare to less than 40% for $k = 1$.)

The vigorous radiation observed in the numerical experiment initialized by the long wave is clearly a result of the change in the dynamical nature of the solution caused by the nonzonality of the mean current. In general, the long part of the spectrum is favored by the radiation if $\alpha \neq 0$, although energetically radiating short waves also develop in the course of nonlinear interactions.

c. Dependence on β

We have observed that the nonzonality of the mean current and the resulting presence of the downstream component β_1 of the planetary vorticity gradient have a large effect on the radiating properties in the problem ([sections 6](#) and [6b](#)). Large β_1 results in the very energetic radiation of the initially trapped short waves of mode 1 for $k = 1$. The ability to radiate energy to regions remote from the jet itself is further enhanced if long waves are considered ($k = 0.25$) on which the x component of the planetary vorticity gradient has especially large influence (see preceding section).

The value of $\beta_1 = \beta \sin \alpha$ in our model is controlled by both the nondimensional planetary vorticity gradient $\beta = L_{\text{jet}}^2 / U$ and the horizontal tilt α . We therefore need to consider the influence of each of the parameters individually on the radiating properties in the model.

Note that the forcing \mathcal{F} in (1) depends only on β_1 , that is, the combined effect of β and the tilt. Investigating the effect of β and α independently will allow us to attribute the radiation to the tilt of the jet rather than to the potential vorticity forcing \mathcal{F} .

We have already studied the case in which β is relatively large, but the tilt is small: $\alpha = 5^\circ$, $\beta = 1$ in [section 5](#). A slightly nonzonal, strong and narrow jet was therefore considered in the experiment, and the planetary vorticity gradient had a small downstream component: $\beta_1 = 0.087$. The comparison with the experiment for $\alpha = 30^\circ$ and the same β ([section 3c](#)) reveals the enforcing effect that larger tilt has on the radiation. But does the tilt by itself or, rather, the related increase in β_1 enhance

the radiation in the latter case? The question is especially important because, as noted, the magnitude of forcing needed for balancing the basic flow $\beta_1 u$ is directly proportional to the value of β_1 .

We try to answer these questions by doing the numerical experiment with smaller β . We will keep β_1 as small as in the case $\beta = 1$, $\alpha = 5^\circ$, but make α as large as in the case $\alpha = 30^\circ$, $\beta = 1$. For the next numerical experiment we consider a smaller value of the planetary vorticity gradient, $\beta = 0.25$ for $k = 1$, $\alpha = 30^\circ$. The downstream component β_1 is small and equals 0.125, making the comparison with the case $\beta = 1$, $\alpha = 5^\circ$ meaningful. If β_1 governs the process of radiation, the two cases will be very similar in radiating properties.

The Fourier coefficients Φ_0 , Φ_1 , and Φ_2 are presented in [Fig. 17](#). The difference with the results for larger β (see [Fig. 12](#)) is apparent.

The x -independent component of the solution reaches finite amplitudes by $t = 48$ and starts to radiate waves long in y to the left from the current. By the end of the numerical experiment, the component reaches very large amplitudes, becoming the largest in amplitude in the set. The change in the x -averaged field is much larger than in the case of larger β . The planetary vorticity gradient acts as a restoring force for Rossby wave oscillations; therefore smaller beta destabilizes the jet even further, leading to the large changes in the x -averaged momentum over the whole domain.

Despite the absence of the corresponding \mathbf{U} velocity, the kinetic energy of component “0” at $t = 96$ is larger than of component “1” ([Fig. 18a](#)). Unlike all cases considered before (see, in particular, [Figs. 13b](#) and [7](#)), the radiating response is dominated energetically by the x -independent component of the solution. Nearly 40% of the total perturbation energy is radiated by this component; one can compare this number to 10% for $\beta = 1$ ([Fig. 13b](#)) in which case the radiation is also very strong.

Component “1” is mainly confined to the region from -2 to 2 until $t = 56$, which can be seen in both [Figs. 17](#) and [18](#). After that, the component slowly extends in the y direction, especially to the right from the jet ([Fig. 17](#)). However, even at $t = 104$ significant amplitudes of the streamfunction are only observed in the interval $[-5, 5]$. The amplitudes are still smaller than those of the component “0.” This slow spreading of the component is different from the vigorous radiation of waves observed, for example, in [section 3d](#).

Nevertheless, we observe the transfer of energy from the jet to the regions that are five times farther from the jet axis than the edge of the jet. Although by the end of the numerical experiment the radiation by component “1” is less energetic than the radiation by component “0,” the corresponding external energy E_1 is still approximately 15% of K_e . The number is only slightly smaller than that for the case $\beta = 1$, $\alpha = 30^\circ$ and is significantly larger than in the case of $\alpha = 5^\circ$ (less than 2.5% in that case; see [Fig. 7](#)).

The remarkable growth in the external part of the kinetic energy in the described case leads us to the conclusion that the main factor in setting the radiation is the nonzonal orientation of the mean current, not the downstream component of the planetary vorticity gradient β_1 and the magnitude of the potential vorticity source $\beta_1 u$, which are both small. Small β leads to the very energetic development of x -averaged component, but slows the radiation of the component “1.”

7. Mode 2

We have already observed in [section 3a](#) that the emergence of the very unstable mode 2 in the course of nonlinear development of mode 1 leads to the weak radiation by the latter. What are the radiating properties of mode 2 alone?

This mode is strongly trapped in the linear problem if the jet is zonal. The radiating properties in the problem change significantly if the horizontal tilt of the jet is made nonzero. The long waves become radiating, although the radiation is weaker than for mode 1. What happens in the nonlinear regime?

In the numerical experiment not presented here, no radiation is found in the case of a zonal jet for $k = 2$. The solution remains trapped to the jet throughout the whole nonlinear development (the problem is integrated until $t = 96$). It is, therefore, the interaction with the shorter wave of mode 1 that produced weak radiation in the experiment described in [section 3a](#).

The next step is to make the mean current nonzonal and observe changes in the radiating properties of the solution. For this purpose, we initialize the model with mode 2 for $k = 1.8$, $\beta = 1$, and $\alpha = 30$. The wave evolves very rapidly because of the very fast initial growth; the growth rate is more than twice as large as that of mode 1 for $k = 1$ (see [Fig. 1](#)). The problem is integrated until $t = 52$.

We turn our attention to the Fourier coefficients of the solution (see [Fig. 19](#)). In the way typical of the nonlinear development in our model, the radiation starts in the form of the x -independent component of the solution at $t = 24$ and occurs for negative y . We note that radiation begins earlier than for the mode 1 because of the faster development of the linear solution. The beginning of the nonlinear equilibration is once again the beginning of the radiative phase in the development.

Component “1.8” dominates the development (Fig. 20a). Unlike mode 1, the nonlinear development of mode 2 does not result in the excitation of the short, very unstable linear waves because the linear problem is stable for k larger than 3β (Fig. 1).

The x dependence of the radiating response develops for $t > 36$, when components “1.8” and “3.6” start to radiate. However, the radiating response formed by component “1.8” decays in space away from the jet region. The radiation still reaches as far as $y = -5$ and $y = 10$ for negative and positive y correspondently by $t = 52$, but the amplitudes are much smaller than those for mode 1.

The energy $E_{1.8}$ of component “1.8” contained in both the external regions is about 5% of the total perturbation kinetic energy K_e (Fig. 20b). Large gradients of the streamfunction compensate the smallness of its amplitude in the value of corresponding energy. Component “3.6” contributes very little (less than 0.5%).

One can recall from the linear problem that even long waves of mode 2 are weakly radiating (see [Kamenkovich and Pedlosky 1996](#)). Despite the absence of spatial trapping of the solution at the long-wave cutoff of the dispersion curve, the process of radiation is significantly less energetic than that for the long waves of mode 1. As we have just observed, nonlinear effects do not significantly change the radiating properties of mode 2; radiation is weak. The difference with the longer nonlinear waves of mode 1, which radiate a significant portion of kinetic energy into the external regions, is apparent.

8. Summary

The present study concerns the ability of a nonzonal ocean current to support unstable disturbances that are not spatially trapped to the current but, rather, are of radiating nature. These radiating instabilities can effectively transfer the kinetic energy of the basic current, initially localized in space, into regions remote from such an energy source. An energetic eddy field can be induced in the far field as a result.

Two main issues are addressed in the study. The first is the difference in radiating and stability properties between a zonal and nonzonal flow. The second is the effects that nonlinear interactions have on the radiating properties of a solution in the finite-amplitude regime. A simple barotropic QG model with a nonzonal current as a basic state is used in the study.

The radiation of short waves that are strongly linearly unstable and trapped during the initial stage of development takes place during the nonlinear equilibration in the model with a nonzonal current. The fast initial growth of those waves, which is the main cause for their spatial trapping, slows significantly during the equilibration and a solution starts to expand in the cross-jet direction.

As in the linear problem ([Kamenkovich and Pedlosky 1996](#)), the difference in the radiating properties between a zonal flow and a nonzonal current is large. The radiation by the zonal flow is weak and takes place as a result of the transient growth of secondary instabilities in the model. In contrast, the radiation is robust and very energetic if the horizontal tilt is different from zero. For $\alpha = 5^\circ$, the radiation starts when initially fast exponential growth significantly slows. The corresponding radiating response is much more energetic than that in the case of the zonal current.

The observed radiation by a nonzonal current is caused by the reduction in the disturbance growth, which happens during the equilibration of solutions. On the other hand, the radiation does not seem to cause the equilibration in the model since the latter also occurs in the case of a zonal current, in which case no energetically significant radiation is found.

A wide spectrum of secondary modes is generated in the course of nonlinear development of a single primary mode as a result of wave-wave interactions. All these components become radiating when they reach finite amplitude. The radiation typically starts in the form of the x -independent component that represents the change in the x -averaged momentum. The other harmonics in x follow; they extend into regions remote from the axis of the basic current, resulting in the complex spatial structure of the radiating response in the far field. The radiating response in the exterior is initially in agreement with the phase speed condition of the linear theory while the amplitudes are still small.

The radiation is especially remarkable when longer waves are considered, since the effect of the downstream component of the planetary vorticity gradient is the largest for those waves [see [Kamenkovich and Pedlosky \(1996\)](#) and [Eq. \(4\)](#)]. For $k = 0.25$, the broad spectrum of vigorously radiating waves is excited, eventually transporting more than 70% of the total perturbation energy into the far field. The radiation starts very quickly, largely because of the small initial growth rate and resulting weak trapping of the linear solution.

The effects of smaller β are also studied in detail. For $\beta = 0.25$, the downstream component of planetary vorticity gradient β_1 is as small as in the case of larger β but smaller tilt ($\beta = 1$ and $\alpha = 5^\circ$). The radiation, however, is significantly stronger. We can conclude that the nonzonal orientation of the current is the main factor controlling the strength of the radiation in the model.

We recall that the forcing, which acts as a vorticity source necessary to balance the mean field, is proportional to β_1

(section 2). That radiation is strong despite the smallness of β_1 demonstrates that the radiation is not directly related to the forcing itself but is, rather, caused by the nonzonal orientation of the mean current. The role of forcing is limited to supporting the nonzonal current.

Although the details of the development depend on the initial conditions used in any particular numerical experiment, the transfer of energy is effective in all cases. A large portion of the perturbation kinetic energy is contained in the far field by the end of all numerical experiments described in the present work.

We have considered only the nonlinear development in the problem initialized with a single Fourier mode. In the more general case in which initial conditions consist of a set of linear waves, the short waves that typically grow faster initially can eventually dominate the development in the region of the jet. The longer nonlinear waves that are more radiating can be either suppressed by those trapped short waves and not produce radiation, or they can continue radiation dominating the far field. In any case, the dynamical properties of both types of modes should change. Those changes are studied in Part II of this study.

Acknowledgments

We would like to thank Glenn Flierl and Roger Samelson for the helpful discussions. The comments from two anonymous reviewers have improved the manuscript greatly. This research was supported in part by National Science Foundation Grant OCE-9301845.

REFERENCES

- Blumberg, A. F., and L. H. Kantha, 1985: Open boundary condition for circulation models. *J. Hydraul. Eng.*, **111** (2), 237–255..
- Fantini, M., and K.-K. Tung, 1987: On radiating waves generated from barotropic shear instability of a western boundary current. *J. Phys. Oceanogr.*, **17**, 1304–1308..
- Flierl, G. R., and V. M. Kamenkovich, 1975: Gulf Stream meandering and Gulf Stream Ring eddy production mechanisms. *Dynamics and the Analysis of MODE-1*, A. R. Robinson, Ed., The MIT Press, 115–118..
- Gill, A. E., J. S. A. Green, and A. J. Simmons, 1974: Energy partition in the large-scale ocean circulation and the production of mid-ocean eddies. *Deep-Sea Res.*, **21**, 499–528..
- Halkin, D., and T. Rossby, 1985: The structure and transport of the Gulf Stream at 73°W. *J. Phys. Oceanogr.*, **15**, 1439–1452..
- Held, I. M., and V. D. Larichev, 1995: A scaling theory for horizontally homogeneous baroclinically unstable flow on a beta plane. *J. Atmos. Sci.*, **52**, 946–952.. [Find this article online](#)
- Hogg, N. G., 1988: Stochastic wave radiation by the Gulf Stream. *J. Phys. Oceanogr.*, **18**, 1687–1701..
- , 1994: Observations of Gulf Stream meander induced disturbances. *J. Phys. Oceanogr.*, **24**, 2534–2545..
- Kamenkovich, I., and J. Pedlosky, 1996: Radiating instability of nonzonal ocean currents. *J. Phys. Oceanogr.*, **26**, 622–643..
- Larichev, V. D., and I. M. Held, 1995: Eddy amplitudes and fluxes in a homogeneous model of fully developed baroclinic instability. *J. Phys. Oceanogr.*, **25**, 2285–2297..
- Malanotte-Rizzoli, P., D. B. Haidvogel, and R. E. Young, 1987: Numerical simulation of transient boundary-forced radiation. Part I: The linear regime. *J. Phys. Oceanogr.*, **17**, 1440–1457..
- , N. G. Hogg, and R. E. Young, 1995: Stochastic wave radiation by the Gulf Stream: Numerical experiments. *Deep-Sea Res.*, **42**, 389–423..
- McIntyre, M. E., and M. A. Wessman, 1978: On radiating instabilities and resonant over-reflection. *J. Atmos. Sci.*, **35**, 1190–1196.. [Find this article online](#)
- Orlanski, I., 1976: A simple boundary condition for unbounded hyperbolic flows. *J. Comput. Phys.*, **21**, 251–269..
- Pedlosky, J., 1975: A note on the amplitude of baroclinic waves in the mid-ocean. *Deep-Sea Res.*, **22**, 575–576..
- , 1977: On the radiation of meso-scale energy in the mid-ocean. *Deep-Sea Res.*, **24**, 591–600..
- Rossby, T., 1987: On the energetics of the Gulf Stream at 73°W. *J. Mar. Res.*, **45**, 59–82..
- Talley, L. D., 1983: Radiating barotropic instability. *J. Phys. Oceanogr.*, **13**, 972–987..
- Wyrki, K., L. Magaard, and J. Hager, 1976: Eddy energy in the oceans. *J. Geophys. Res.*, **81**, 2641–2646..

APPENDIX

9. Open Boundary Conditions

For the open boundary conditions we use the modified Orlandi boundary conditions (5). For the finite-difference form, we first write (5) with unknown propagation speed c (Blumberg and Kantha 1985):

$$\frac{\psi_N^t - \psi_N^{t-2}}{2\Delta t} + \frac{c}{\Delta y} \left[\frac{1}{2} (\psi_N^t + \psi_N^{t-2}) - \psi_{N\mp 1}^{t-1} \right] = -\frac{\psi_N^{t-2}}{T_f}. \quad (\text{A1})$$

The index N represents a grid point on the open boundary. The upper sign in the double-sign expressions corresponds to the boundary on the right, and the lower sign corresponds to the boundary on the left. Here x dependence is omitted from all expressions in this section.

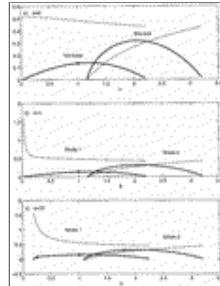
The next step is to determine the propagation speed c . To do that, we write the above expression now for a grid point neighboring to the boundary $N \mp 1$, rather than at the boundary itself, and without the damping term. We get the expression for c (Orlandi 1976):

$$c = \frac{\psi_{N\mp 1}^t - \psi_{N\mp 1}^{t-2}}{\frac{1}{2} (\psi_{N\mp 1}^t + \psi_{N\mp 1}^{t-2}) - \psi_{N\mp 2}^{t-1}} \frac{\Delta y}{2\Delta t}. \quad (\text{A2})$$

As is pointed out in Orlandi (1976), we need also to make sure that the disturbance propagates to the boundary. Therefore, c should be set to zero if expression (A2) gives negative number for the right boundary and positive value for the left boundary.

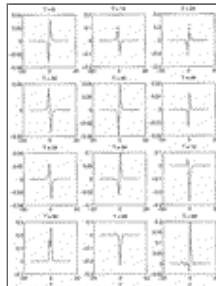
The above conditions have proven to work very well for most cases in our model. The experiments show in particular that open boundary conditions result in much less reflection than if sponge layers were used.

Figures



Click on thumbnail for full-sized image.

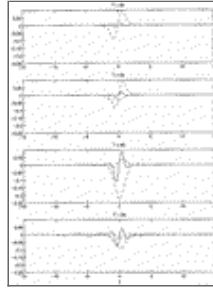
Fig. 1. The phase speeds c_r (thin lines) and growth rates ω_i (heavy lines) as functions of k for mode 1 and mode 2 for $\beta = 1$ and (a) $\alpha = 0^\circ$, (b) $\alpha = 5^\circ$, and (c) $\alpha = 30^\circ$. The marks on the curves show the choices of parameters for different numerical runs.



Click on thumbnail for full-sized image.

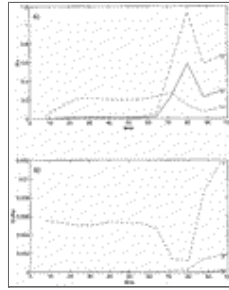
Fig. 2. The streamfunction as function of y for $x = 1.4$, $\alpha = 0^\circ$: $k = 1$ and $\beta = 1$. The time corresponding to a snapshot is given on

the top of a panel. The linear solution is shown by the dashed lines in the first three plots. The scales are different between panels.



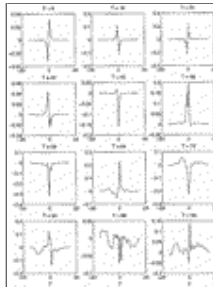
Click on thumbnail for full-sized image.

Fig. 3. The Fourier coefficients Φ_0 (solid lines), Φ_1 (dashed lines), and Φ_2 (dashed–dotted lines) of the streamfunction as functions of y : $\alpha = 0^\circ$, $k = 1$, and $\beta = 1$. Corresponding times are given on the top of each panel.



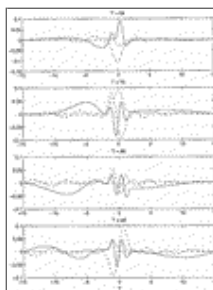
Click on thumbnail for full-sized image.

Fig. 4. Kinetic energy corresponding to each Fourier component vs time: (a) K_{k_n} (energy integrated over the whole domain) and (b) E_{k_n} (energy integrated from $-\infty$ to -2 and from 2 to ∞) divided by the total energy K_e for $\alpha = 0^\circ$, $k = 1$, and $\beta = 1$. Component numbers are shown on the plot.



Click on thumbnail for full-sized image.

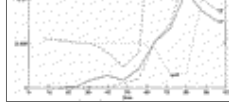
Fig. 5. The streamfunction as function of y . As in Fig. 2 but for $x = 1.37$ and $\alpha = 5^\circ$: $k = 1$ and $\beta = 1$.



Click on thumbnail for full-sized image.

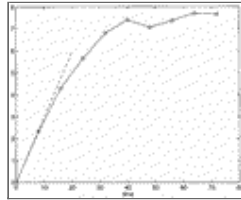
Fig. 6. The Fourier coefficients Φ_0 (solid lines), Φ_1 (dashed lines), and Φ_2 (dashed–dotted lines) of the streamfunction as functions of y for $\alpha = 5^\circ$: $k = 1$ and $\beta = 1$.





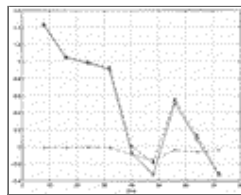
[Click on thumbnail for full-sized image.](#)

Fig. 7. External kinetic energy E_{k_n} corresponding to each Fourier component vs time. As in the lower panel of [Fig. 4](#) but for $\alpha = 5^\circ: k = 1$ and $\beta = 1$; $(E_0 + E_1 + E_2)/K_e$ for the zonal jet is shown by the dotted line (marked by $\alpha = 0$).



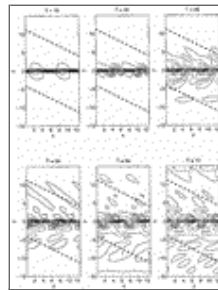
[Click on thumbnail for full-sized image.](#)

Fig. 8. The logarithm of perturbation kinetic energy for $\alpha = 30^\circ: k = 1$ and $\beta = 1$ vs time; $\log(K_e(t)/K_e(0))$ is shown by the solid line with open dots, and $2\omega_e t$ is shown by the dashed line.



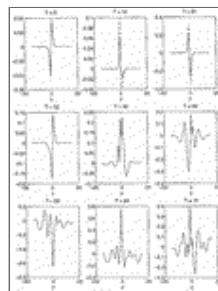
[Click on thumbnail for full-sized image.](#)

Fig. 9. The ratios of the terms in the energy equation to the total perturbation energy: $d[K_e(yb)/K_e]/dt$ is shown by the solid line with circles, F_{brt}/K_e is shown by the dashed line with stars, and flux/K_e is shown by the dashed-dotted line with crosses; $y_b = 2$, $\alpha = 30^\circ$, $k = 1$, and $\beta = 1$.



[Click on thumbnail for full-sized image.](#)

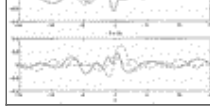
Fig. 10. Two-dimensional contour plots of the total streamfunction $\Psi(y) + \psi(x, y)$. Corresponding times are given on the top of each plot. Heavy dashed lines are parallel to the latitude circles. Mode 1: $k = 1$, $\beta = 1$, and $\alpha = 30^\circ$.



[Click on thumbnail for full-sized image.](#)

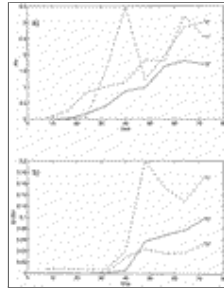
Fig. 11. The streamfunction as a function of y . As in [Fig. 2](#) but for $x = 1.37$ and $\alpha = 30^\circ: k = 1$ and $\beta = 1$.





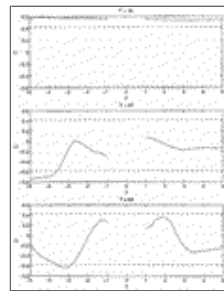
Click on thumbnail for full-sized image.

Fig. 12. The Fourier coefficients Φ_0 (solid lines), Φ_1 (dashed lines), and Φ_2 (dashed-dotted lines) of the streamfunction as functions of y for $\alpha = 30^\circ$: $k = 1$ and $\beta = 1$.



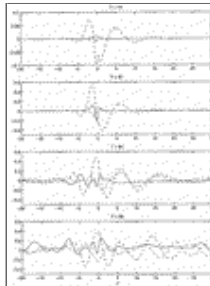
Click on thumbnail for full-sized image.

Fig. 13. Kinetic energy corresponding to each Fourier component. As in Fig. 4 but for $\alpha = 30^\circ$: $k = 1$ and $\beta = 1$.



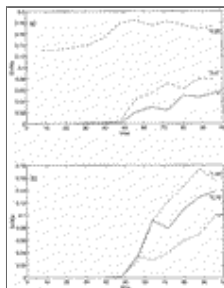
Click on thumbnail for full-sized image.

Fig. 14. The function $c_1(y, t)$ defined by Eq. (10) as a function of y for different times, $k = 1$: $\beta = 1$ and $\alpha = 30^\circ$. The upper and lower bounds on the allowed for radiation phase speed set by the phase speed condition (9) is shown by the dashed lines. The jet region $[-1, 1]$ is not shown.



Click on thumbnail for full-sized image.

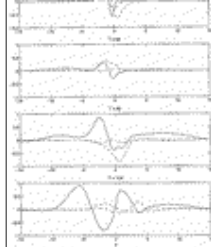
Fig. 15. The Fourier coefficients Φ_0 (solid lines), $\Phi_{0.25}$ (dashed lines), and $\Phi_{0.5}$ (dashed-dotted lines) of the streamfunction as functions of y for $\alpha = 30^\circ$: $k = 0.25$ and $\beta = 1$. Corresponding times are given on the top of each panel.



Click on thumbnail for full-sized image.

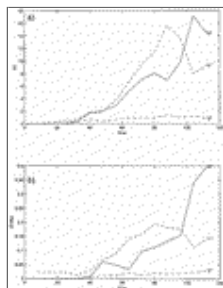
Fig. 16. External kinetic energy corresponding to each component divided by total perturbation energy K_e for (a) components “0,” “0.25,” and “0.5”; (b) “0.75,” “1,” and “1.25”: $\alpha = 30^\circ$, $k = 0.25$, and $\beta = 1$. Component numbers are shown in the plot.





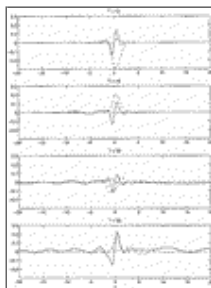
Click on thumbnail for full-sized image.

Fig. 17. The Fourier coefficients Φ_0 (solid lines), Φ_1 (dashed lines), and Φ_2 (dashed–dotted lines) of the streamfunction as functions of y for $\beta = 0.25$, $k = 1$, and $\alpha = 30^\circ$.



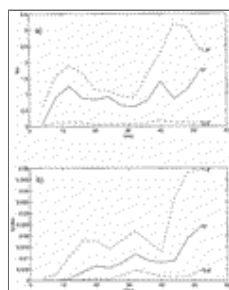
Click on thumbnail for full-sized image.

Fig. 18. Kinetic energy corresponding to each Fourier component. As in Fig. 4 but for $\beta = 0.25$, $\alpha = 30^\circ$, and $k = 1$.



Click on thumbnail for full-sized image.

Fig. 19. The Fourier coefficients Φ_0 (solid lines), $\Phi_{1.8}$ (dashed lines), and $\Phi_{3.6}$ (dashed–dotted lines) of the streamfunction as functions of y . Corresponding times are given on the top of each panel. Mode 2: $\alpha = 30^\circ$, $k = 1.8$, and $\beta = 1$.



Click on thumbnail for full-sized image.

Fig. 20. External kinetic energy corresponding to each Fourier component divided by total perturbation energy K_e for $\alpha = 30^\circ$, $k = 1.8$, and $\beta = 1$. As in Fig. 4 but for mode 2.

* Woods Hole Oceanographic Institution Contribution Number 9439.

+ Current affiliation: Department of Earth, Atmospheric and Planetary Sciences, Massachusetts Institute of Technology, Cambridge, Massachusetts.

Corresponding author address: Dr. Igor V. Kamenkovich, Massachusetts Institute of Technology, Bldg. E40, Room 263, Cambridge, MA 02139.

E-mail: igor@gyre.mit.edu



© 2008 American Meteorological Society [Privacy Policy and Disclaimer](#)
Headquarters: 45 Beacon Street Boston, MA 02108-3693
DC Office: 1120 G Street, NW, Suite 800 Washington DC, 20005-3826
amsinfo@ametsoc.org Phone: 617-227-2425 Fax: 617-742-8718
[Allen Press, Inc.](#) assists in the online publication of *AMS* journals.